A New Parameterization for Shallow Cumulus Convection and Its Application to Marine Subtropical Cloud-Topped Boundary Layers. Part I: Description and 1D Results

CHRISTOPHER S. BRETHERTON, JAMES R. MCCAA, AND HERVÉ GRENIER

Department of Atmospheric Sciences, University of Washington, Seattle, Washington

ABSTRACT

A new parameterization of shallow cumulus convection is presented. The parameterization consists of a mass flux scheme based on a buoyancy-sorting, entrainment–detrainment plume model. The mass flux scheme is coupled to a 1.5-order turbulence closure model with an entrainment closure for convective boundary layers. Model performance is verified using single-column-model simulations at relatively high vertical resolution of pure trade-cumulus convection and a cumulus to stratocumulus transition. Mixing rates, cloud cover, and vertical flux profiles, as deduced from previously published large-eddy simulation studies, are well reproduced by the parameterization. The model is used to demonstrate that height variations of lateral mixing rates can be successfully captured by a simple implementation of a buoyancy-sorting mechanism in the updraft cloud model. A companion paper describes the implementation of the scheme in a mesoscale model.

1. Introduction

Shallow cumulus convection, in which the cumuli are not deep enough for precipitation processes to play a major role in cloud development, has long been recognized as an important climate process. By venting air from the surface mixed layer toward the free troposphere, shallow convection strongly influences boundary layer depth, temperature, relative humidity, cloud cover, and winds. Shallow cumulus clouds are the most abundant of all tropical clouds (Johnson et al. 1999), and in the subtropics a sizable fraction of stratocumulus are also underlain and sustained by shallow cumulus convection (Norris 1999). Hence, shallow cumulus clouds significantly impact the earth's radiation budget.

Shallow cumulus convection has been parameterized in large-scale models using an effective eddy diffusivity (e.g., Tiedtke et al. 1988) or a moist adjustment scheme (e.g., Betts 1986). However, here we focus on the parameterization of shallow cumulus using the mass flux approach. This involves coupling a simple cloud model to an algorithm for specifying an upward mass flux through the cloud bases. Historically, the cloud model has been either a spectrum of entraining–detraining cloud updrafts (Arakawa and Schubert 1974), or updrafts and downdrafts (Johnson 1976), a spectrum of

subcloud-scale drafts (Emanuel 1991), or a single-plume bulk entraining–detraining updraft–downdraft (e.g., Tiedtke 1989; Gregory and Rowntree 1990; Kain and Fritsch 1990; Bechtold et al. 2001). Each cloud model is built on a different set of parametric assumptions regarding lateral exchange between the cloud and environment.

Relatively few studies have examined the performance of cumulus parameterizations applied to shallow convection. Shallow cumulus convection is in some ways simpler than deep convection. Precipitation processes are by definition less important, and typically the cumuli rise from a dry convective subcloud layer that is fairly homogeneous both horizontally and vertically. However, turbulent mixing processes are particularly important for shallow convection, and many deep convective parameterizations do not perform well on shallow convection because they typically employ inadequate formulations of turbulent mixing in and around cumuli.

In this paper, our goal is to improve simulation of marine subtropical and tropical low clouds in a mesoscale model. We present a new parameterization for shallow cumulus convection; its coupling to a planetary boundary layer (PBL), or more precisely, a turbulent mixing scheme (Grenier and Bretherton 2001); the implementation of the two parameterizations in a mesoscale model; and single-column tests for subtropical and tropical marine cloud-topped boundary layers. In a companion paper (McCaa and Bretherton 2004), we present three-dimensional regional simulations of subtropical

Corresponding author address: Dr. Christopher Bretherton, Dept. of Atmospheric Sciences, University of Washington, Box 351640, Seattle, WA 98195-1640.
E-mail: breth@atmos.washington.edu

stratocumulus and shallow cumulus convection in the northeast and southeast Pacific Ocean. Our new parameterization is based on a buoyancy-sorting single-plume model similar to that of Kain and Fritsch (1990, hereafter KF90), with cloud-base mass flux controlled by a convective-inhibition-based scheme. In the remainder of the introduction, we provide some context for our approach.

The defining assumption of a single-plume mass flux scheme is that the flux model

$$\rho \overline{w'\psi'} \approx M_u(\psi_u - \overline{\psi}) \qquad (1)$$

gives an adequate estimate of ensemble-averaged convective fluxes in cumulus layers. In (1), M_u is the cloud mass flux (with units of kg m^{-2} s^{-1}); ψ_u is the bulk updraft-average value of some conserved variable ψ, which changes with height because of mixing of updraft and environmental air; and $\overline{\psi}$ is the value of ψ in the environment. The simplification (1) is bold and open to obvious criticisms—the cumulus ensemble is at any time composed of a spectrum of clouds of different depths and different stages in their life cycle, and each could is a complex, turbulent, amalgam of updrafts and downdrafts (e.g., Krueger et al. 1997). Nevertheless, Siebesma and Cuijpers (1995, hereafter SC95), using large-eddy simulation (LES) studies of shallow cumulus, found that (1) can provide a surprisingly reasonable approximation to LES-simulated ensemble-mean fluxes. However, for a parameterization based on (1) to give a proper estimate of fluxes, the cloud model also must correctly predict the mass flux and the bulk updraft properties with height.

Turbulent mixing of the cloud updraft with its environment is critically important in determining how M_u and ψ_u vary with height. We follow the classical approach of idealizing this as lateral entrainment of environmental air into a homogeneous updraft and detrainment of updraft air into the environment, though we recognize that this is only a metaphor for the time-averaged mixing processes occuring during cloud growth and decay. We follow KF90's approach of implementing buoyancy sorting in this framework, as discussed in section 2e. The cloud mass flux obeys the mass continuity equation

$$\frac{\partial}{\partial z}(M_u) = E - D, \qquad (2)$$

and the updraft thermodynamic properties obey a dilution equation (Betts 1973). In (2), E and D are the lateral entrainment and detrainment mass fluxes per unit height. Siebesma and Holtslag (1996) have shown that if E and D are chosen to match LES-inferred values, single-column model (SCM) simulations of shallow cumulus convection can give realistic thermodynamic profiles. Parametric formulations for E and D broadly consistent with the LES results have been proposed (Siebesma and Holtslag 1996; Grant and Brown 1999). However, the appropriate sensitivities for E and D to

convective-layer and subcloud-layer depths and environmental profiles remain unclear.

Telford (1975) introduced *buoyancy sorting* as an idealized two-step model of lateral mixing between cloud and environment. In the first step, turbulence creates a spectrum of mixtures between undilute updraft and environmental air. Next, negatively buoyant mixtures descend to their level of neutral buoyancy, while positively buoyant mixtures are incorporated into the cumulus updraft. Aircraft observations of cumulus congestus (Paluch 1979) and some LESs (Reuter and Yau 1987; Lin and Arakawa 1997a,b; Carpenter et al. 1998) support aspects of this model, though ambiguities in interpreting the observations remain (Taylor and Baker 1991). Raymond and Blyth (1986) introduced a conceptual cloud model based on buoyancy sorting, and cumulus parameterizations proposed by Emanuel (1991) and KF90 incorporated simplified forms of buoyancy sorting.

The parameterization we introduce uses a modified version of the KF90 buoyancy sorting entraining–detraining plume model. At each height, lateral mixing of updraft and environmental air is assumed to generate a specified distribution of mixtures. Mixtures that are sufficiently negatively buoyant (as explained in section 2c) are rejected, corresponding to detrainment of the updraft component of the mixture. Positively buoyant mixtures are incorporated into the updraft, corresponding to entrainment of the environmental part of the mixture. In describing our scheme, we find it useful to distinguish between "lateral mixing," entrainment (incorporation and complete mixing of environmental air into the updraft), and detrainment (incorporation and complete mixing of updraft air into the environment). We note that in other buoyancy-sorting schemes, for example, the Raymond–Blyth (1986) scheme in which all lateral mixing is between the environment and undilute cloud-base air, "entrainment" often is used differently, as a synonym for lateral mixing.

A second major issue in cumulus parameterization is specifying whether there is convection ("triggering"), and if so, how much ("closure"). The closure in deep convection schemes typically ties cumulus mass flux to some measure of conditional instability (e.g., KF90) or moisture convergence (e.g., Tiedtke 1989). However, another approach, where the triggering and mass flux closure are controlled by the strength of the weak stable layer capping the subcloud layer (Emanuel and Raymond 1992), is particularly attractive for shallow cumulus convection due to the well-defined subcloud convective layer. We describe a method for specifying the mass flux based on the convective inhibition at the top of the subcloud layer and the amount of turbulence within it.

While we were in advanced stages of developing this parameterization, Bechtold et al. (2001) and von Salzen and McFarlane (2002) introduced cumulus parameterizations that each have features in common with our proposed approach. Bechtold et al.'s bulk updraft

scheme includes KF90-style buoyancy sorting and also penetrative mixing into cumuli above their level of neutral buoyancy, but unlike our scheme uses a CAPE-controlling mass flux closure and is also directly applicable to deep convection. Von Salzen and McFarlane incorporate an idealized life cycle of lateral and penetrative mixing due to individual cumuli and compare different assumptions about buoyancy sorting.

The new cumulus mass flux parameterization is introduced in section 2. Section 3 presents SCM results and sensitivity tests for two idealized cases. A summary follows in section 4.

2. Model formulation

The SCM used in this study consists of a one-dimensional version of the fifth-generation Pennsylvania State University–National Center for Atmospheric Research (Penn State–NCAR) Mesoscale Model (MM5), version 2 (Grell et al. 1994). The 28-layer 1D model contains physical parameterizations identical to those in the 3D model, but the vertical velocity, surface pressure, and geostrophic wind are specified. The KF90 deep convection scheme (which is active only for a cumulus layer diagnosed to have a depth exceeding 4 km) was used in addition to the new shallow convection parameterization. The Grenier and Bretherton (2001, hereafter GB01) PBL scheme was implemented as described below. The Community Climate Model Version 2 (CCM2) radiation scheme was used but was modified to include a statistical cloud fraction for stratiform clouds, to compute the radiative effects of convective clouds, and to assume maximum random overlap for longwave radiation (McCaa 2001). The statistical cloud fraction is used only within the radiation package. The cloud microphysics scheme was adapted from the Colorado State University Regional Atmospheric Modeling System (RAMS) model (Pielke et al. 1992) and includes the modifications for precipitation from stratocumulus proposed by Chen and Cotton (1987). The numerical concentration of cloud droplets (CCN) is assumed to be 100 cm^{-3}; a sensitivity study to a different CCN concentration will also be discussed.

Within the PBL and shallow convective parameterizations, the prognostic quantities are the liquid water potential temperature $\theta_l = \theta - q_l L_v / \Pi c_p$ (Betts 1973) and the total water mixing ratio $q_t = q_v + q_l$, both assumed to be conserved for nonprecipitating moist adiabatic processes, and the horizontal wind components u and v. Here, θ is the potential temperature, q_l and q_v the liquid water and water vapor mixing ratios, L_v the latent heat of vaporization, c_p the specific heat of dry air at constant pressure, and Π the Exner pressure function. Vertical advection is handled using the MM5 centered-difference scheme, except for a modification proposed by GB01 across the inversion capping a convective PBL.

The main characteristics of our implementation of the GB01 boundary layer scheme are presented below, followed by a description of the convective mass flux scheme and how the two are coupled.

a. PBL/layer turbulence model

The GB01 model is a 1.5-order turbulent closure model (TCM) based on the Mellor and Yamada (1982) formulation. Each grid column is vertically discretized into cells labeled with integer indices j increasing from bottom to top, separated by interfaces $j + 1/2$ at which fluxes between cells are computed. If a turbulent layer (set of contiguous grid cells) in a given grid column is diagnosed to be "convective," that is, if the buoyancy flux is positive somewhere within it, an entrainment closure is used instead of the TCM to compute the turbulent entrainment fluxes at its top. In this study, GB01's "restricted inversion" implementation is used. The top of the convective layer is restricted to lie at an interface between grid cells and is treated as a discontinuity in thermodynamic properties and momentum. Since there will always be an associated discontinuous increase of virtual temperature with height, we refer to the convective-layer top as an inversion. GB01 used a moist Richardson number threshold to diagnose the tops of convective layers, which can lead to oscillation in the depths of convective layers with weak inversions. We instead choose the top of the convective layer as the lowest interface $k + 1/2$ satisfying the inequality

$$(N^2 l^2)_{k+1/2} \geq -0.5(N^2 l^2)_{\text{avg}}, \qquad (3)$$

where N is the buoyancy frequency, l is the master turbulent length scale, and the subscript "avg" indicates an average over all interfaces $j + 1/2$, $j < k$ within the interior of the convective layer. This criterion approximately corresponds in the GB01 formulation to a condition that the buoyancy flux anywhere in the interior of a convective layer not be more negative than -0.5 of the layer-mean buoyancy flux, a condition inspired by the flux profiles of dry convective PBLs and LES decoupling in stratocumulus-capped PBLs (Stevens 2000). The master turbulent length scale is slightly modified from GB01 and is set to

$$l = \min(\kappa z, c_1 l_d), \qquad (4)$$

where $\kappa = 0.4$ is the von Karman constant, l_d is the depth of the convective layer, and $c_1 = 0.1$ is a parameter controlling the level of turbulent kinetic energy (TKE) in the boundary layer that is chosen as in GB01.

As proposed in GB01, the eddy diffusivity K_h and viscosity K_m at the inversion are computed as

$$K_{h,m} = w_e \Delta_{\text{inv}} z, \qquad (5)$$

where w_e is the entrainment velocity of the convective layer, and $\Delta_{\text{inv}} z$ represents the distance between the grid cell midpoints below and above the inversion. The entrainment velocity is calculated as

$$w_e = \frac{A e_{\mathrm{inv}}^{3/2}}{l \Delta_{\mathrm{inv}} B_v}, \qquad (6)$$

where A is the entrainment efficiency, e_{inv} is the TKE at the inversion, and $\Delta_{\mathrm{inv}} B_v$ is the "inversion strength," defined as the buoyancy jump across the inversion. Elsewhere, eddy-mixing coefficients are computed as

$$K_{h,m} = l S_{h,m} \sqrt{e}, \qquad (7)$$

with $S_{h,m}$ the stability functions specified in Galperin et al. (1988).

In this approach, an important concept is the *ambiguous* layer, which is the grid cell above the nominal entrainment interface, and in which the true convective-layer top lies. It is considered to contain a combination of mixed-layer and free-tropospheric air. For the vertical advection scheme to be fully consistent with this approach, corrections to the vertical advective fluxes at the base and top of the ambiguous layer are applied, following GB01. In the MM5, which uses a centered-differencing advection scheme, applying such corrections is crucial to ensuring good performance of the GB01 scheme.

We allow several vertically stacked turbulent layers in an individual column. Even though we refer to the GB01 "PBL" scheme, this is really a layer-oriented vertical turbulent mixing scheme. For instance, in a parameterized "decoupled" or "cumulus coupled" cloud-topped boundary layer (CTBL), there will be a surface-forced convective layer (the true PBL), from which shallow cumulus convection is permitted, and a second radiatively driven convective layer containing the stratocumulus cloud and into which the shallow cumuli may be detraining. When we refer to the CTBL, we mean the subcloud layer combined with any overlying shallow cumulus and stratocumulus, and the "trade inversion" refers to the statically stable layer capping the CTBL.

b. Shallow convective mass flux scheme

The mass flux scheme is based on an entraining–detraining single-plume model. An entire population of clouds is represented by a single updraft that exchanges air with the environment through lateral entrainment and detrainment. The convective mass flux M_u (in units of kg m^{-2} s^{-1}) is defined as

$$M_u = \rho_u \sigma_u w_u, \qquad (8)$$

where ρ_u is the updraft air density, σ_u is the fractional area of the grid box supporting cumulus updrafts, and w_u is the convective updraft velocity. Assuming that storage of some variable ψ within the cloud ensemble represented by the single updraft can be neglected $[\partial(\sigma_u \psi_u)/\partial t = 0]$, the diagnostic equations for the mass flux and the bulk updraft ψ_u can be written (Yanai et al. 1973)

$$\frac{\partial M_u}{\partial z} = E - D, \quad \text{and} \qquad (9)$$

$$\frac{\partial}{\partial z}(\psi_u M_u) = X_\psi + S_\psi M_u, \qquad (10)$$

where X_ψ represents the net lateral exchange of ψ between the updraft and the environment, and S_ψ is a source term. The source term includes parameterized pressure gradient effects on updraft momentum of the form $S_\psi = 0.7 \partial \overline{\psi}/\partial z$ for $\psi = u$ or v, following Gregory et al. (1997). There is also a crude precipitation sink for the updraft total water $q_{t,u}$, which removes all updraft cloud water in excess of an arbitrary critical value $q_{l,\mathrm{crit}} = 1$ g kg^{-1} and increases the updraft liquid water potential temperature $\theta_{l,u}$ accordingly.

The lateral exchange X_ψ is parameterized as

$$X_\psi = E\overline{\psi} - D\psi_u, \qquad (11)$$

where E and D are the rates at which mass is respectively entrained into the updraft with properties $\overline{\psi}$ and detrained with properties ψ_u. The overbar is used throughout to indicate the mean properties of the environment.

Defining ε and δ as the fractional entrainment and detrainment rates (per meter)

$$E = \varepsilon M_u \quad \text{and} \quad D = \delta M_u, \qquad (12)$$

and manipulating (9), (10), (11), and (12) leads to the updraft dilution equations

$$\frac{\partial M_u}{\partial z} = M_u(\varepsilon - \delta), \qquad (13)$$

$$\frac{\partial \psi_u}{\partial z} = \varepsilon(\overline{\psi} - \psi_u) + S_\psi. \qquad (14)$$

The vertical velocity equation for the updraft is given by

$$\frac{1}{2}\frac{\partial}{\partial z}w_u^2 = B_u - \varepsilon w_u^2 - P, \qquad (15)$$

where B_u is the buoyancy of the updraft relative to the environment, defined as

$$B_u = g\frac{\theta_{v,u} - \overline{\theta_v}}{\overline{\theta_v}}, \qquad (16)$$

and P represents the drag on upward acceleration resulting from updraft-induced pressure perturbations and the growth of subplume turbulence within the updraft. Previous authors (Simpson and Wiggert 1969; Gregory 2001; Siebesma et al. 2003) have parameterized P as a linear combination the first two terms on the right-hand side of (15), yielding

$$\frac{1}{2}\frac{\partial}{\partial z}w_u^2 = aB_u - b\varepsilon w_u^2, \qquad (17)$$

where b is a drag coefficient, and a is a virtual mass coefficient introduced by Simpson and Wiggert (1969).

There remains uncertainty as to the appropriate formulation, and we have chosen to use simply a drag coefficient, specifying $a = 1$ and $b = 2$.

In appendix A, a discretization of these equations is presented that allows their vertical integration without constraints on the vertical resolution or the value of the entrainment and detrainment rates.

c. Formulation for lateral entrainment and detrainment

Entrainment and detrainment rates are critical parameters of mass flux schemes (Tiedtke 1989; Gregory and Rowntree 1990; SC95). In the widely used "entraining plume" model, turbulent mixing of environmental air with updraft air is treated as a one-way process in which environmental air is laterally entrained into the updraft at some specified rate per unit height, regardless of the buoyancy of any intermediate mixtures produced [Arakawa and Schubert (1974), though they did consider a spectrum of entraining plumes that can mimic aspects of buoyancy sorting]. However, following the buoyancy-sorting approach of KF90, we assume that lateral mixing between a horizontally homogeneous updraft and a horizontally homogeneous environment occurs at a specified mixing rate per unit height, generating an assumed spectrum of mixtures. Buoyancy sorting is used to determine which mixtures are incorporated into the updraft and which are rejected. Rates of entrainment of environmental air into the updraft and detrainment of updraft air into the environment are obtained by integrating over the mass-mixing distributions making up the two types of mixtures, yielding an entraining–detraining plume model (9) for the updraft properties.

Our model differs from KF90 in the specification of the mixing rate, in our assumption of a uniform (instead of Gaussian) mixing distribution, and in basing the entrainment calculation on the upward momentum of mixed parcels in addition to their buoyancy. KF90 followed similarity theory for thermals and related a height-independent lateral mixing rate to R^{-1}, where R is the typical updraft diameter. We scale R with the height H of the top of cumulus layer at the previous model time step and specify a *fractional* mixing rate

$$\varepsilon_0 = c_0/H, \tag{18}$$

with c_0 fixed empirically to 15 to best simulate LES-derived entrainment/detrainment rates in the trade-cumulus case discussed in section 3a. For $H = 2000$ m, this is equivalent at cloud base to $R = 40$ m in the KF90 formulation. For newly active convection, H is set to the height z above the surface. Siebesma (1998) also argued for a formulation similar to (18) in which entrainment rate scales inversely with cumulus height.

In a thin layer of thickness δz, equal parts $\varepsilon_0 M_u \delta z$ of updraft and environmental air are involved in the lateral mixing process that creates a spectrum of mixtures. This yields a total mixing mass flux $2\varepsilon_0 M_u \delta z$. Let χ be the
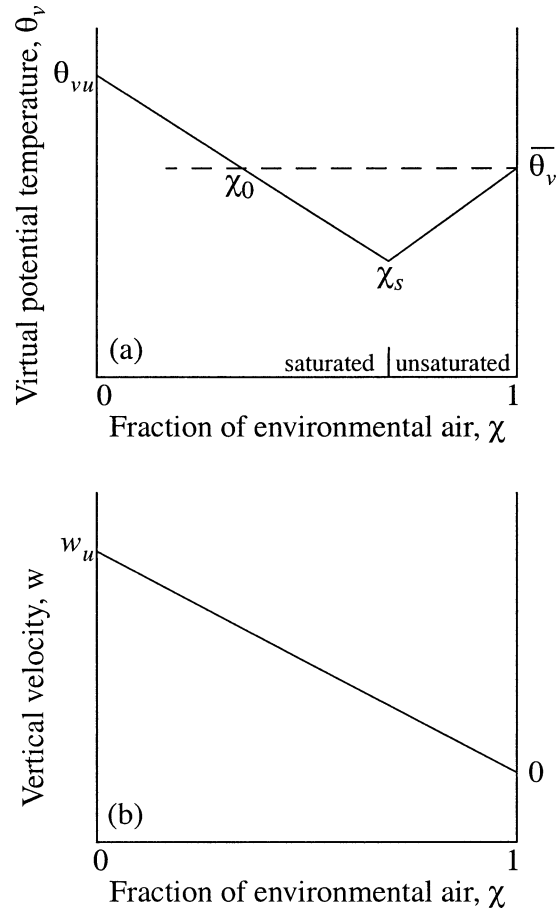

FIG. 1. (a) Virtual temperatures for typical fractional mixtures of saturated updraft and unsaturated environmental air, where χ_s denotes the fraction where the mixture is exactly saturated, and χ_0 denotes the fraction below which mixtures are positively buoyant with respect to the environment. (b) Initial vertical velocities for the same mixtures.

mixing fraction of environmental air in the mixtures, where χ ranges from 0 for undilute updraft to 1 for pure environmental air. Let $q(\chi)$ be the mass-mixing probability distribution function for mixtures with mixing fraction χ. We follow Raymond and Blyth (1986) rather than KF90 and choose $q(\chi)$ to be a uniform distribution such that all mixtures between undiluted updraft and environment are equally likely to be found. There is no observational evidence to favor either choice, and the uniform distribution simplifies calculations. Figure 1a plots virtual temperatures for typical fractional mixtures of saturated updraft and unsaturated environmental air. In a conditionally unstable environment, the unsaturated mixtures and more dilute cloudy mixtures will be negatively buoyant. As long as the updraft is positively buoyant, a range of mixtures $0 \leq \chi < \chi_0$ will also be positively buoyant.

According to the KF90 buoyancy-sorting mechanism, all negatively buoyant parcels (those with $\chi > \chi_0$) are immediately rejected from the updraft. However, neg-

atively buoyant cloudy parcels are observed in shallow cumulus (Taylor and Baker 1991), and the LES results of SC95 show that cumulus updrafts include substantial fractions (up to 40%) of negatively buoyant air. Furthermore, this buoyancy-sorting scheme produces an excessive decrease of mass flux with height when applied to the test case of section 3a if all negatively buoyant mixtures are rejected. Therefore, momentum is also considered here in the computation of entrainment and detrainment.

Momentum is considered to be linearly mixed between updraft and environment, as shown in Figure 1b, and in the absence of further entrainment, each rising mixed parcel with negative buoyancy will travel some distance l_e before its velocity becomes 0. The fraction of mixtures χ_c considered to be entrained into the plume is determined by retaining all positively buoyant mixtures (all of which are saturated) and those negatively buoyant saturated mixtures that continue upward in excess of some critical eddy-mixing distance l_c related to the convective-scale height H by

$$l_c = c_1 H, \tag{19}$$

where $c_1 = 0.1$ is an empirical constant, chosen to optimize the trade-cumulus simulation of section 3a. This assumes that within a height l_c after mixing, each rising mixture loses its identity by becoming fully entrained into the updraft. A description of the computation of χ_c is included in appendix B.

Given the critical mixing fraction, the net amount of environmental air entrained in the updraft is

$$2\varepsilon_0 M_u \int_0^{\chi_c} \chi q(\chi) \, d\chi = \varepsilon_0 M_u \chi_c^2. \tag{20}$$

Likewise, the updraft air to be detrained after mixing is simply

$$2\varepsilon_0 M_u \int_{\chi_c}^1 (1 - \chi) q(\chi) \, d\chi = \varepsilon_0 M_u (1 - \chi_c)^2. \tag{21}$$

Hence, the effective lateral entrainment rate is $\varepsilon = \varepsilon_0 \chi_c^2$, while the effective detrainment rate is $\delta = \varepsilon_0 (1 - \chi_c)^2$. The mass flux continuity equation (13) with the chosen frequency and mass distribution of mixtures is

$$\frac{1}{M_u} \frac{\partial M_u}{\partial z} = \varepsilon - \delta = \varepsilon_0 (2\chi_c - 1). \tag{22}$$

For χ_c larger than 1/2, the mass flux increases with height. This will occur if the environment is close to saturation and/or if the updraft buoyancy and liquid water content are large. For nonbuoyant updrafts, rapid detrainment is forced to occur as χ_c is small or 0.

d. Updraft properties at cloud base

Updraft properties at the base of the cumulus layer provide the lower boundary condition required to in-

tegrate the dilution equation (14). Aircraft observations (Pennell and LeMone 1974) and LES results (Nicholls et al. 1982; Lin 1999; Siebesma et al. 2003) show that updraft buoyancy at the cumulus cloud base is negligible, but that the updrafts have humidity excesses of a few tenths of grams per kilogram and correspond to humidities found in the surface layer. Therefore, the cloud-base updraft mixing ratio $q_{t,u}$ is chosen to be the surface-layer specific humidity:

$$q_{t,u} = \overline{q_{t,1}}. \tag{23}$$

Given $q_{t,u}$, the updraft virtual potential temperature $\theta_{v,u}$ at cloud base is set equal to the lowest value of $\overline{\theta_v}$ within the PBL. This ensures that the updraft is neutrally or weakly negatively buoyant at the cumulus base. The cloud-base updraft liquid water potential temperature $\theta_{l,u}$ may then be diagnosed from $\theta_{v,u}$ and $q_{t,u}$.

Cumulus updrafts are assumed to originate at the PBL top (constrained to lie on a flux level). This ensures that for the important case of a stratocumulus-capped PBL below a strong inversion, cumulus convection will not initiate at the stratocumulus cloud base and compete with the turbulence parameterization. The cumulus base is taken to be the higher of the updraft LCL (which will generally lie between flux levels) and the PBL top. Updraft air is assumed to move from the PBL top to the cumulus base without entrainment or detrainment, conserving $\theta_{l,u}$ and $q_{t,u}$.

e. Cloud-base mass flux

Our mass flux closure is based on the assumption that a buoyant cumulus cloud can only form if the source air has sufficient vertical velocity to penetrate the weak inversion atop the subcloud layer and reach its level of free convection. For air with given thermodynamic properties, a critical vertical velocity w_c can be computed such that undilute source air leaving the mixed layer with $w > w_c$ will reach its level of free convection and continue upward. To do so accurately requires detailed information about the relative heights of the inversion, the lifting condensation level (LCL) of cumulus updrafts, and the level of free convection (LFC), as well as the vertical structure of the environmental properties in the vicinity.

Figure 2 shows a plot of virtual potential temperature for source air and environmental air near the inversion. It can be seen that the source air is negatively buoyant for some distance above the inversion. Within this region any potential plume air traveling upward will decelerate. The critical velocity w_c is defined such that source air released at the inversion with velocity w_c will arrive at the LFC with zero velocity. Convective inhibition (CIN) is indicated by the shaded area in Fig. 2 and is computed in the model by summing components of the shaded area. Conserved variables are used to estimate the environmental θ_v profile from its gridpoint values using the piecewise linear finite-volume interpretation presented in
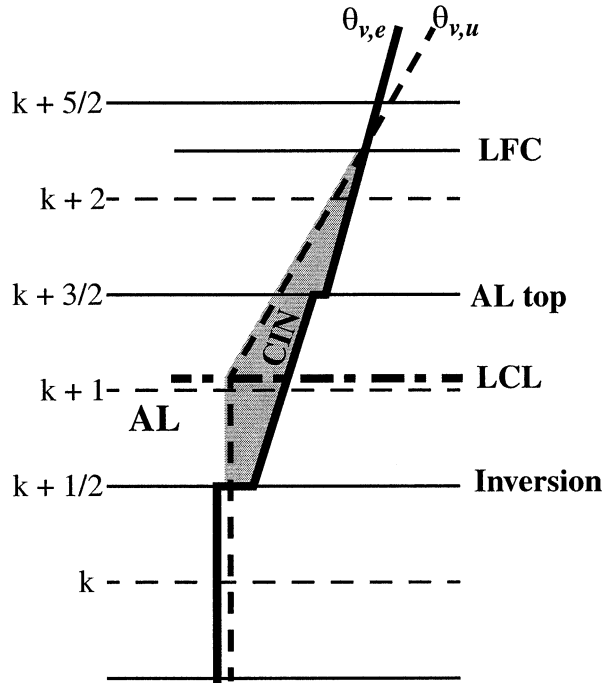
FIG. 2. Calculation of CIN from the virtual potential temperatures of source air (thick dashed line) and environmental air (thick solid line) near the inversion at the top interface of the subcloud convective layer. On the lhs are labels denoting model flux levels (thin solid lines) and thermodynamic levels (thin dashed lines). Average-conserving piecewise linear thermodynamic profiles are used within each model layer. AL denotes the "ambiguous layer" $k + 1$ lying just above the inversion.

GB01. The updraft θ_v is calculated at the inversion, LCL, and flux levels, and is linearly interpolated in between these points. With a typical model vertical grid spacing of hundreds of meters, the environmental θ_v profile will certainly be underresolved, with the LCL and LFC likely lying within the "ambiguous layer" that lies above the inversion flux level. In this case, the computed CIN should not be taken too literally, but still acts as a control valve that forces the thermodynamic profiles near cloud base to adjust consistently with the parameterized convection. The calculation of CIN is discussed in more detail in appendix C.

Given the CIN and neglecting any entrainment into the updraft below the LFC, the critical velocity, derived from the updraft vertical velocity equation (17), is $w_c = \sqrt{2a(\text{CIN})}$, where $a = 1$ is the virtual mass coefficient from Eq. (17). The cumulus mass flux is now specified to be the amount of source air that impinges on the inversion with a velocity in excess of w_c. A statistical model is used to estimate the distribution of vertical velocity at the inversion. The distribution of w is assumed to be Gaussian, with a variance $\overline{w'^2}$ estimated as

$$\overline{w'^2} = k_f e_{\text{avg}}, \qquad (24)$$

where e_{avg} is the average TKE in the subcloud mixed layer predicted by the PBL scheme, and $k_f = 0.5$ is an

empirical parameter describing the partitioning of TKE between horizontal and vertical motions at the subcloud layer inversion, chosen from LESs of shallow cumulus-capped PBLs presented by Siebesma et al. (2003).

This results in a vertical velocity distribution of the form

$$f(w) = \frac{1}{\sqrt{2\pi k_f e_{\text{avg}}}} \exp\left(-\frac{w^2}{2 k_f e_{\text{avg}}}\right), \qquad (25)$$

which can be integrated from w_c to infinity to yield the areal fraction at the inversion of updrafts that will penetrate the LFC:

$$\sigma_{\text{inv}} = \int_{w_c}^{\infty} f(w)\, dw = \frac{1}{2} \operatorname{erfc}\left(\frac{w_c}{\sqrt{2 k_f e_{\text{avg}}}}\right). \qquad (26)$$

Integrating $w\overline{\rho_{\text{inv}}} f(w)$ over the same range yields the updraft mass flux at the inversion

$$M_{u,\text{inv}} = \overline{\rho_{\text{inv}}} \int_{w_c}^{\infty} w f(w)\, dw$$

$$= \overline{\rho_{\text{inv}}} \sqrt{\frac{k_f e_{\text{avg}}}{2\pi}} \exp\left(-\frac{w_c^2}{2 k_f e_{\text{avg}}}\right), \qquad (27)$$

where $\overline{\rho_{\text{inv}}}$ is the density of source air at the LFC. In the case of $\sigma_{\text{inv}} < 0.001$, the mass flux is set to zero and no other computations are performed.

The updraft velocity at the inversion is obtained from (28),

$$w_{u,\text{inv}} = \frac{M_{u,\text{inv}}}{\sigma_{\text{inv}} \overline{\rho_{\text{inv}}}}. \qquad (28)$$

Since no entrainment or detrainment is assumed to occur between the inversion and the LCL, $M_{u,\text{LCL}} = M_{u,\text{inv}}$. Above the LCL, entrainment and detrainment are computed as described above, with the fractional layer between the LCL and the next model flux level treated as an ordinary but thin model layer.

The specification of the mass flux closure has a form similar to that proposed by Mapes (2000), who postulated that convective mass flux should vary as $\exp(-\text{CIN/TKE})$. The present formulation has a similar behavior, with an arguably cleaner theoretical basis.

f. Formulation for cumulus penetrative mixing

As a convective plume reaches its level of neutral buoyancy (LNB), its momentum causes it to continue upward until negative buoyancy drives its vertical velocity to 0. In the model, this may occur within the layer where the buoyancy first becomes negative, or at some higher level. When mixing occurs between environmental air and updraft air above its LNB, all mixed parcels are negatively buoyant, and their negative buoyancy is enhanced by evaporation, suggesting that they will sink back toward the LNB before detraining—a

process Wyant et al. (1997) called penetrative entrainment. Note that they were referring to vertical entrainment of air down across the trade inversion via overshooting cumuli—to avoid confusion with our prior use of the word entrainment we will instead call this "penetrative mixing." They and others (e.g., de Roode and Bretherton 2003) have examined the penetrative mixing process in LES-simulated shallow cumulus ensembles. Though a fully convincing synthesis of mixing dynamics above the LNB has not yet been achieved, our approach follows Wyant et al. (1997) in spirit.

As described in detail in appendix D, penetrative mixing is handled in the model by first finding the highest flux interface $k_{LNB} - 1/2$ at which updraft buoyancy is positive (i.e., such that the LNB is in the overlying grid cell). We then use (17) to calculate the depth of updraft overshoot above level $k_{LNB} - 1/2$. For simplicity, penetrative mixing in the "overshoot zone" above $k_{LNB} - 1/2$ is treated analogous to lower levels in the updraft, as lateral mixing between the overshooting updraft and the environment. The rate of lateral mixing in the overshoot zone is specified as

$$\varepsilon_i = r_p \varepsilon_0. \tag{29}$$

Here ε_0 is taken from (18), and $r_p = 10.0$ is an empirical penetrative mixing enhancement factor parameter that crudely accounts for differences between penetrative and lateral mixing and is chosen to optimize the model simulation of the stratus to trade-cumulus transition of section 3b. All updraft-environment mixtures created in the overshoot zone are negatively buoyant, and we assume they are all detrained below the overshoot zone in cell $k_{LNB} - 1$.

g. Coupling with the boundary layer model

A critical aspect of this work is to achieve proper coupling between our shallow cumulus scheme and our PBL scheme. Unlike in deep precipitating convection where buoyancy-driven downdrafts reach the surface, downdrafts do not penetrate below the cloud base in nonprecipitating cumulus convection (Raga et al. 1990). The cumulus convection vents mass from the surface-driven subcloud convective layer, which is compensated by entrainment of air down into the PBL through the weak subcloud inversion. The problem is how to consistently represent these processes in a gridpoint model that does not explicitly compute the boundary layer mass budget.

In the present model, cumulus updraft air is removed from the PBL model's *ambiguous* layer, even though the updraft properties (see section 2d) are different than the mean properties of that layer. The necessary transports to bring air up to the PBL top are considered part of the PBL scheme, not part of the cumulus circulation itself. This is tantamount to assuming that cumulus updrafts are not affecting the turbulent structure of the PBL beneath them; the assumption is supported by the statistical similarity of the subcloud mixed layer to a dry convective boundary layer that is not overlain by cumuli (Siebesma et al. 2003). However, for numerical stability, if the updraft total water mixing ratio $q_{t,u}$ at the cloud base exceeds that of the ambiguous layer (AL), the deficit $M_{u,LCL}(q_{t,u} - \overline{q_{t,AL}})$ is drawn evenly from throughout the mixed layer. This implies a somewhat artificial moisture flux within the subcloud layer associated with the cumulus roots that is 0 at the surface but increases linearly with height up to the AL top. The total moisture flux within the subcloud layer is the sum of this moisture flux and that predicted by the turbulence scheme; the latter is usually dominant in practice (e.g., see Fig. 5 later).

Neglecting vertical advection for clarity, the budget of a conservative variable ψ in the AL therefore obeys

$$\left(\frac{\partial}{\partial t}\overline{\psi}\right)_{AL} = \frac{-w_e\Delta_{inv}\overline{\psi} - (\overline{M}_{u,top}/\rho_{inv})(\psi_{u,top} - \overline{\psi_{top}})}{z_{top} - z_{inv}}, \tag{30}$$

where the subscript "top" indicates the top of the ambiguous layer, and $\overline{\psi_{top}}$ is the environmental ψ advected down through the AL top by compensating subsidence. We take $\overline{\psi_{top}} = \overline{\psi}_{AL+1}$, the layer-mean environmental ψ for the model layer above the AL. Equation (30) illustrates the counteracting effects of entrainment into the PBL and cumulus convection on the AL budget. From (30), ones notes that the amount of air vented out of the ambiguous layer is $M_{u,top}$. This is different from (and usually slightly less than) $M_{u,LCL}$, as some entrainment and detrainment occurs between the LCL (not a flux level) and z_{top}.

The closure for $M_{u,LCL}$ (section 3e) ensures a strong feedback between the cloud-base mass flux and the strength of the transition layer that helps maintain the top of the subcloud mixed layer realistically near to the updraft LCL. If the stratification across the transition layer is initially small, the cloud-base mass flux will be large. Compensating subsidence will strengthen the transition-layer inversion and increase CIN, reducing $M_{u,LCL}$ to a sustainable level. Stiffness of the closure is a potential issue since small changes in the sounding near the cloud base can cause larger relative impacts on CIN.

h. Numerical considerations

The stability of the shallow cumulus parameterization is affected by vertical resolution and time step. The computation of CIN and to a lesser extent, penetrative mixing, are "stiff," that is, very sensitive to the vertical thermodynamic profiles. However, the proposed method is adequate for stable performance at resolutions of 200 m, and limited sensitivity studies we have done do not show a strong resolution dependence of vertical thermodynamic profiles within the cumulus layer. For time steps exceeding 3 min, the CIN computation at this ver-

tical resolution leads to spurious oscillations in cumulus mass flux.

The exact formulation of the CIN should not affect overall model performance as long as the cloud-base mass flux is ultimately controlled primarily by cloud-layer feedbacks. For longer time steps, we are experimenting with less stiff mechanisms of keeping the LCL just above the top of the subcloud mixed layer and CIN-bypassing approaches (e.g., Grant and Brown 1999). The CIN calculation also may require modification for satisfactory performance with alternate PBL schemes, which might lead to different thermodynamic structures near the top of the subcloud layer.

3. Case studies and results

The mass flux model coupled to the TCM is tested on two cases of marine cumulus convection previously simulated by LES models, one involving trade cumulus and the other involving a stratocumulus to cumulus transition.

a. Pure trade wind cumulus conditions: BOMEX

The Barbados Oceanography and Meteorology Experiment (BOMEX) field campaign took place over the Atlantic Ocean in 1969 (Holland and Rasmusson 1973; Nitta and Esbensen 1974). A subperiod of BOMEX, consisting of a 3-day-long undisturbed period of non-precipitating trade-cumulus clouds, has been used to generate initial conditions and forcings for LES models (SC95; Siebesma et al. 2003, hereafter S03). LES simulations of this case have already proved useful for testing and modification of parameterizations for large-scale models (Siebesma and Holtslag 1996; Grant and Brown 1999).

1) EXPERIMENTAL SETUP

The initial conditions and forcings imposed are similar to the ones prescribed by SC95 and S03 for the fifth Global Water and Energy Experiment Cloud System Studies Working Group 1 (GCSS-WG1) intercomparison (Datasets needed to initialize and force the model can be obtained online at http://www.knmi.nl/~siebesma/gcss/bomex.html), with one significant deviation. In S03, the surface heat and moisture fluxes were specified. For multiday integrations such as ours, this leads to drift of the boundary layer thermodynamic profiles. We instead compute the surface fluxes from the surface winds, temperature, and humidity using the Tropical Ocean Global Atmosphere Coupled Ocean–Atmosphere Response Experiment (TOGA COARE) flux algorithm (Fairall et al. 1996). This introduces a feedback between the surface layer and the ocean that removes the drift, without significantly changing the fluxes from the values prescribed in S03. The SCM is integrated for 144 h with a vertical
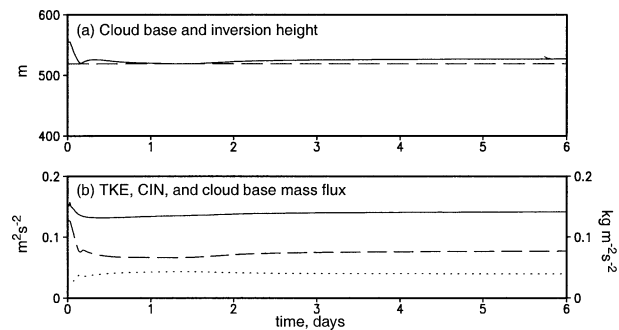

FIG. 3. Time series data from the BOMEX simulation. From top to bottom are (a) cumulus cloud base (solid) and inversion height (dashed); and (b) mixed-layer average TKE (solid), CIN (dashed), and cloud-base mass flux (dotted).

grid spacing of approximately 200 m and a time step of 3 min.

2) TIME SERIES

The coupling between the mass flux scheme and the TCM should maintain the base of the cumulus layer z_{LCL} slightly above, and "coupled" to, the mixed-layer inversion. Figure 3 displays the time evolution of selected model variables near the cloud base. After a rapid adjustment from the initial state, the model slowly evolves for the first day of the simulation, after which it reaches equilibrium. Since the top of the surface-driven mixed layer is constrained to be at a model flux layer, and the simulation remains close to the initial profile, the mixed-layer depth is constant. As expected, z_{LCL} remains above z_{inv}. The CIN equilibrates to approximately 0.08 m^2 s^{-2}, one-half of the convective-layer averaged TKE, and the cloud-base mass flux settles down to about 0.04 kg m^{-2} s^{-1}. The cloud-base mass flux closure, its numerical implementation, and the coupling between the TCM and the mass flux scheme appear to operate stably and as planned at this grid spacing and time step. In the following section, model output is averaged over the last 48 h of the simulation to generate mean profiles.

3) MEAN PROFILES

Figure 4 shows the mean profiles of temperature and specific humidity averaged over hours 72 to 144 of the simulation. The hash marks on the right-hand side of this and subsequent plots indicate the flux levels of the model. During this period there is little change in any of the cloud fields, as suggested by the time series of variables near the cloud base. The properties and depth of the subcloud mixed layer are quite close to the initial conditions. Within the convective layer, there is an increasing negative temperature bias with height, capped by a compressed inversion. The equilibrium water vapor profile also displays sharpened gradients across the trade and subcloud inversions and is drier than the initial pro-
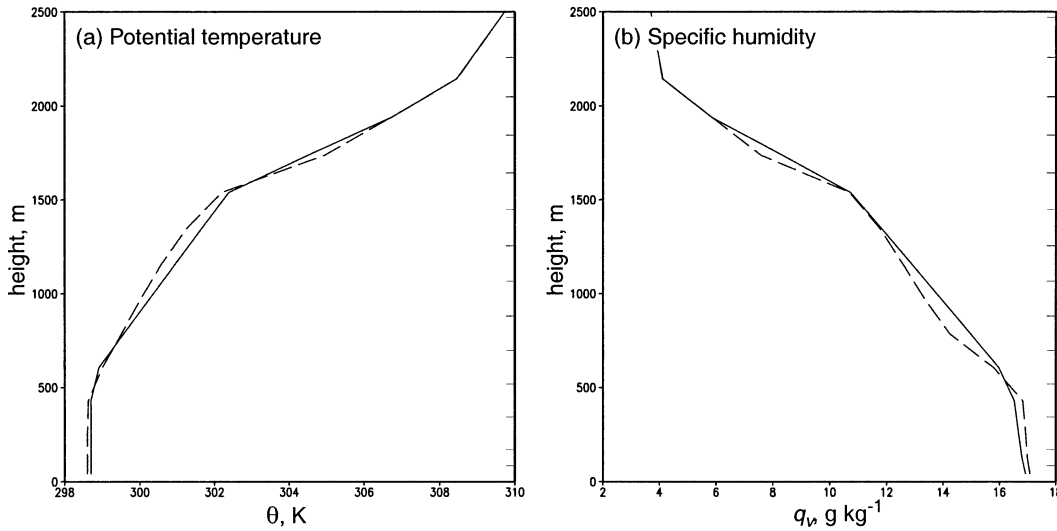
FIG. 4. Profiles of (a) potential temperature and (b) water vapor specific humidity from the BOMEX simulation, for the initial state (solid) and mean state over hours 72 to 144 (dashed).

file in the lower part of the convective layer. The sharpened trade inversion is due to the penetrative mixing formulation, which detrains no updraft air above the level of neutral buoyancy for the bulk updraft. The sharpened subcloud inversion in the model may reflect a smearing of the initial (observed) sounding associated with horizontal undulations in the transition-layer height.

Figure 5 shows fluxes of conserved variables obtained from the combined scheme and the contribution to these fluxes from the shallow cumulus scheme. The TCM
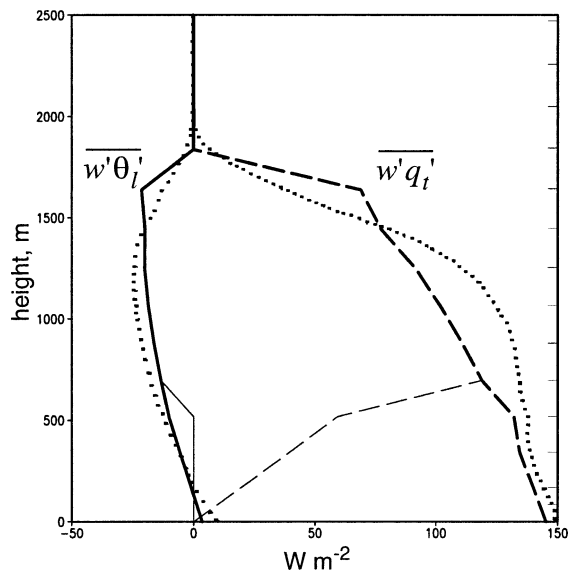

FIG. 5. Time-averaged flux profiles from the BOMEX simulation for q_l (thick solid) and q_t (thick dashed). Also shown are flux contributions from the shallow cumulus scheme (thin solid and thin dashed). The dotted lines indicate the mean turbulent flux profiles from the LES intercomparison of Siebesma et al. (2003).

contribution is the difference between the curves. Also shown are the mean turbulent flux profiles from the LES intercomparison of S03. The simulated profiles are in agreement with the LES results with regard to magnitude and structure but show a sharper trade inversion. Approximately half of the total surface moisture flux is deposited into the single-model layer defining the inversion. The shallow cumulus scheme is responsible (somewhat artificially) for a fraction of the moisture flux even within the PBL. This fraction ranges from 0 at the surface to about half at the PBL top.

SC95 introduced several statistical sampling methods for examining LES moist convective fields, including a "cloud" decomposition (saturated grid cells), a more restrictive "updraft" decomposition (saturated grid cells with positive w), and a "core" decomposition (buoyant saturated grid cells with positive w). The decomposition conceptually closest to the bulk updraft model presented here is the updraft decomposition. SC95 found that the updraft decomposition produced the most accurate description of the fluxes of conserved variables, though it performed poorly for nonconserved variables and did not produce entrainment and detrainment rates nor a mass flux as consistent with observations as did the core decomposition. We will compare incloud profiles from our SCM with updraft decomposition-based results presented in SC95. When these are not available, we use the cloud decomposition results of S03. S03 did not show updraft decomposition results, but below the trade-inversion base more than 90% of the cloud is updraft, so the cloud and updraft decompositions give similar results.

The SCM simulations produce a mass flux profile, shown in Fig. 6(a), that is close in magnitude and structure to the updraft decomposition of SC95. The monotonic decrease of the cloud mass flux with height is in
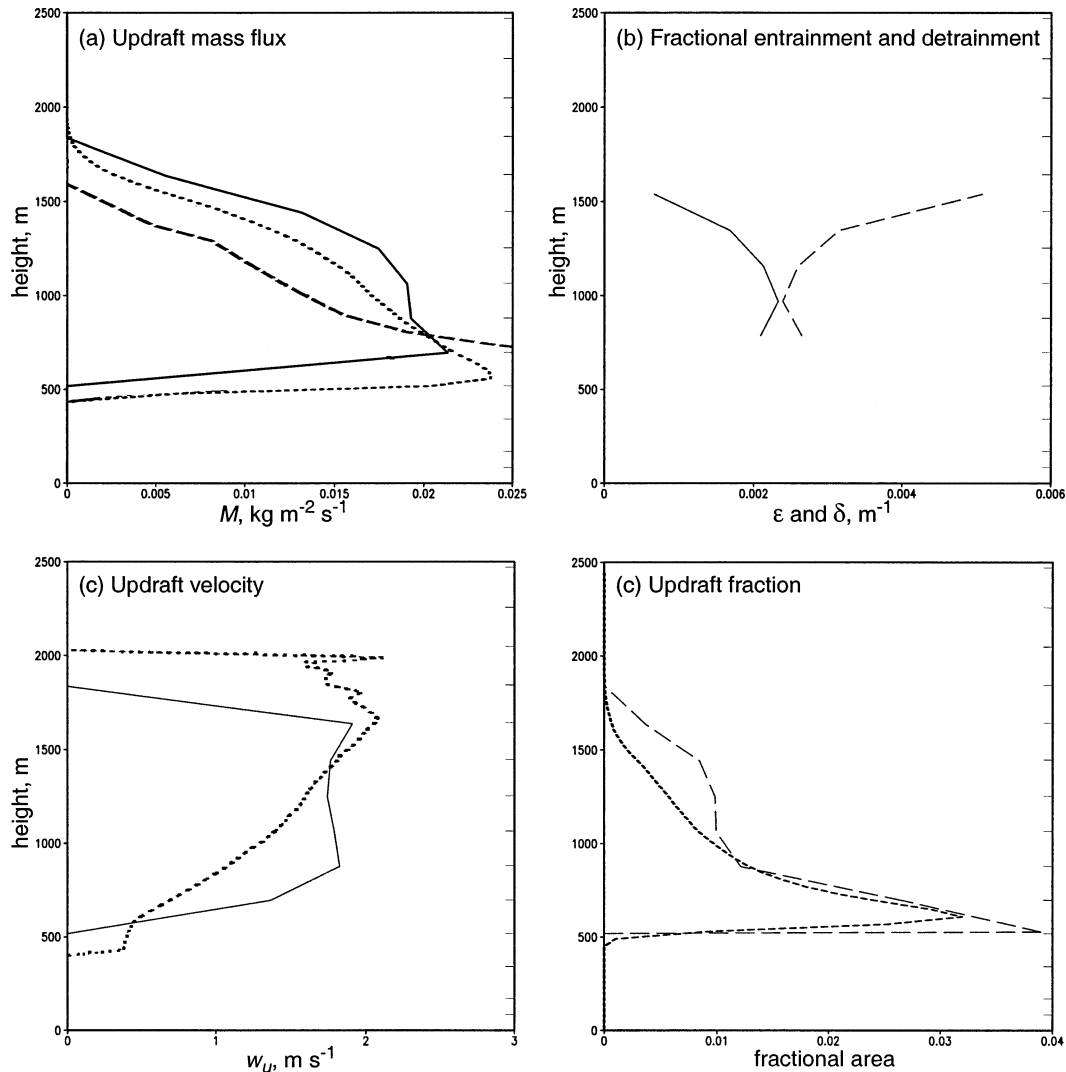
FIG. 6. Time-averaged profiles from the BOMEX simulation for (a) updraft mass flux from MM5 at flux levels (solid), SC95 updraft decomposition (dotted), and Esbensen (1978) analysis of observations; (b) MM5 updraft fractional entrainment (solid) and detrainment (dashed) rates; (c) updraft vertical velocity from MM5 (solid) and from SC95 updraft decomposition (dotted); (d) updraft cloud fraction from MM5 (long dashed) and S03 cloud decomposition fraction (short dashed).

agreement with the LES results and with an analysis of BOMEX observations (Esbensen 1978) in which budget calculations were used to partition the observed heat and moisture fluxes across an ensemble of entraining plume cumuli with a spectrum of entrainment rates. That study showed that comparatively few updrafts in a cumulus field reach higher levels. Correspondingly, as shown in Fig. 6b, the MM5-parameterized detrainment rate δ exceeds the entrainment rate ε at each level. The profile of ε has a distorted parabolic shape, with a maximum of 2.2 km^{-1} in the lower part of the moist convective layer, near 1000 m. The profile of δ shows a variation inverse to ε, with a minimum of 2.3 km^{-1} at 1000 m. The profiles of ε and δ reflect the values of

the critical mixing fraction, which reach a maximum near 1000 m, then decreases to 0 at the trade inversion.

Figure 6c shows the simulated updraft vertical velocity, which reaches approximately 1.9 m s^{-1} near 1000 m, above which it is nearly constant. Below the trade-inversion base (1600 m), our vertical velocity profile is in fair agreement with the updraft decomposition of the SC95 LES analysis. The mass flux and vertical velocity profiles determine the updraft areal fraction, shown in Fig. 6d, which decreases from a maximum of 0.04 at cloud base to less than 0.01 at 1000 m. Also shown is the fractional area of the cloud decomposition from S03, which displays roughly the same structure and magnitude. Above the trade-inversion base, the LES results
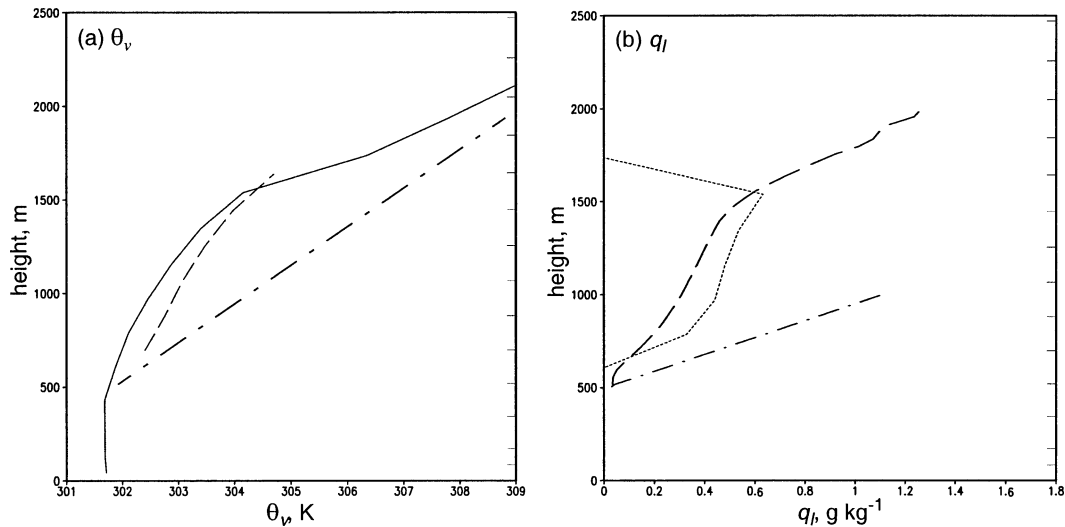
FIG. 7. Time-averaged profiles from the BOMEX simulation for (a) environmental q_v (solid) and updraft q_v (dashed), with undilute adiabatic updraft ascent shown as a dash–dotted line; and (b) liquid water mixing ratio for the mean updraft (short dashed) and LES (S03) "cloud decomposition" (long dashed). The dash–dotted line in (b) shows the expected liquid water mixing ratio for undilute adiabatic ascent from 500 m.

are dominated by a few vigorous overshooting cumulus updrafts of very small fractional area. The conditional sampling no longer reflects the evolution of a typical cumulus updraft reaching the trade inversion, which is closer to what our model is representing. Thus increasing levels of disagreement should be expected between the SCM and LES results as one moves higher into the trade inversion.

The virtual potential temperature of the environment and the bulk updraft is shown in Fig. 7a. The updraft remains positively buoyant by a fraction of a degree throughout the lower part of the cumulus layer and only becomes negatively buoyant upon penetrating the inversion. Figure 7b shows the profile of liquid water mixing ratio within the updraft. Because of entrainment dilution, the updraft liquid water is much less than that of adiabatic ascent and is in agreement with the S03 LES results up to the base of the trade inversion. The corresponding evaporation of condensed liquid water cools the updraft, keeping its lapse rate subadiabatic. The equilibrium liquid water path of 7 g m^{-2} (estimated from cumulus liquid water mixing ratios and fractional areas at the model flux levels) is also in good agreement with the S03 results.

b. Stratocumulus to trade cumulus transition

Krueger et al. (1995) and Wyant et al. (1997, hereafter W97) described idealized two-dimensional LESs representative of the boundary layer evolution of the subtropical northeast Pacific Ocean. They modeled the deepening and warming of a stratocumulus layer under an initially strong inversion advecting over increasing sea surface temperature. We compare our SCM to W97's simulation, which is "Lagrangian" in the sense that the

sea surface temperature rises at 1.5 K day^{-1} over a 10-day period, with the intent to model a column of boundary layer air as it moves with the mean wind across the sea, while the tropospheric temperature, humidity, winds, and subsidence remain constant throughout the simulation. At the start of W97's simulation, a stratocumulus-capped mixed layer forms, then decouples after a few days to form cumulus under thinning stratocumulus, and finally the stratocumulus disappear to leave a pure trade-cumulus-capped PBL.

This case is useful to understand the behavior of a SCM over a large range of salient subtropical forcings and was simulated here to investigate the sensitivity of the coupling between the subcloud and cloud layers to changes in environmental conditions.

1) FORCINGS AND INITIAL CONDITIONS

The forcings and initial conditions used in this simulation are similar to those prescribed in W97. However, surface fluxes were computed using the TOGA COARE flux algorithm (Fairall et al. 1996) rather than W97's prescribed transfer coefficients. Radiative fluxes were computed with the modified CCM scheme described above, including a diurnal cycle of insolation, and the model was integrated for 10 days.

2) SIMULATION RESULTS

Figure 8 shows a time–height cross section of gridscale cloud water, cumulus mass flux, and TKE (predicted by the turbulence parameterization) for our simulation. There are three distinct phases corresponding to a well-mixed stratocumulus-capped CTBL, a period of cumulus rising into stratocumulus, and a trade-cu-
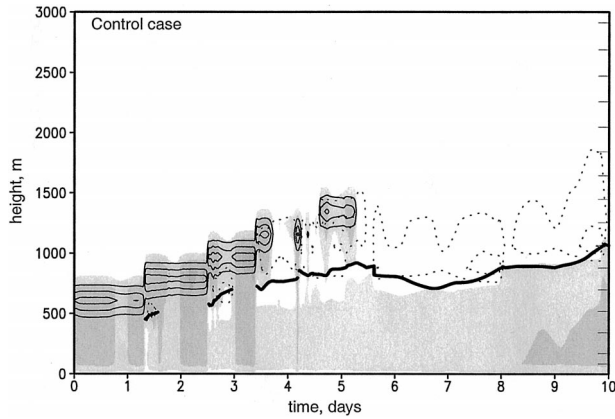
FIG. 8. Lagrangian warming case: time evolution of TKE (shaded; contour interval 0.2 m^{-2} s^{-2}), cloud water (thin black contours; interval 0.1 g kg^{-1}), cumulus mass flux (dotted contours; interval 0.02 kg m^{-2} s^{-1}), and cumulus cloud base (heavy solid line).

mulus regime. The CTBL, initially capped by a resolved cloud at 600 m, deepens and at day 2.5 begins to decouple into a surface mixed layer and a radiatively driven turbulent stratocumulus layer, separated by a layer in which TKE is small. The shallow cumulus scheme is briefly active at day 1.3–1.4, then becomes persistently active in the decoupled regime. The CTBL deepens by approximately 400 m over the following 3 days, at which point the explicitly resolved stratocumulus dissipates. For the remainder of the simulation, only the cumulus cloud field is present, and TKE is restricted to the subcloud mixed layer. The cumulus cloud-top height remains constant over the next 3 days, then deepens again to 1800 m by day 10. These features are in general agreement with W97, though the cloud breakup is more sudden and the inversion height rises less steadily.

Vertical profiles of θ_l, θ_v, q_t, and q_l are shown in Fig. 9. The simulation is qualitatively similar to the LES of W97. The inversion strength weakens from 14 K at the
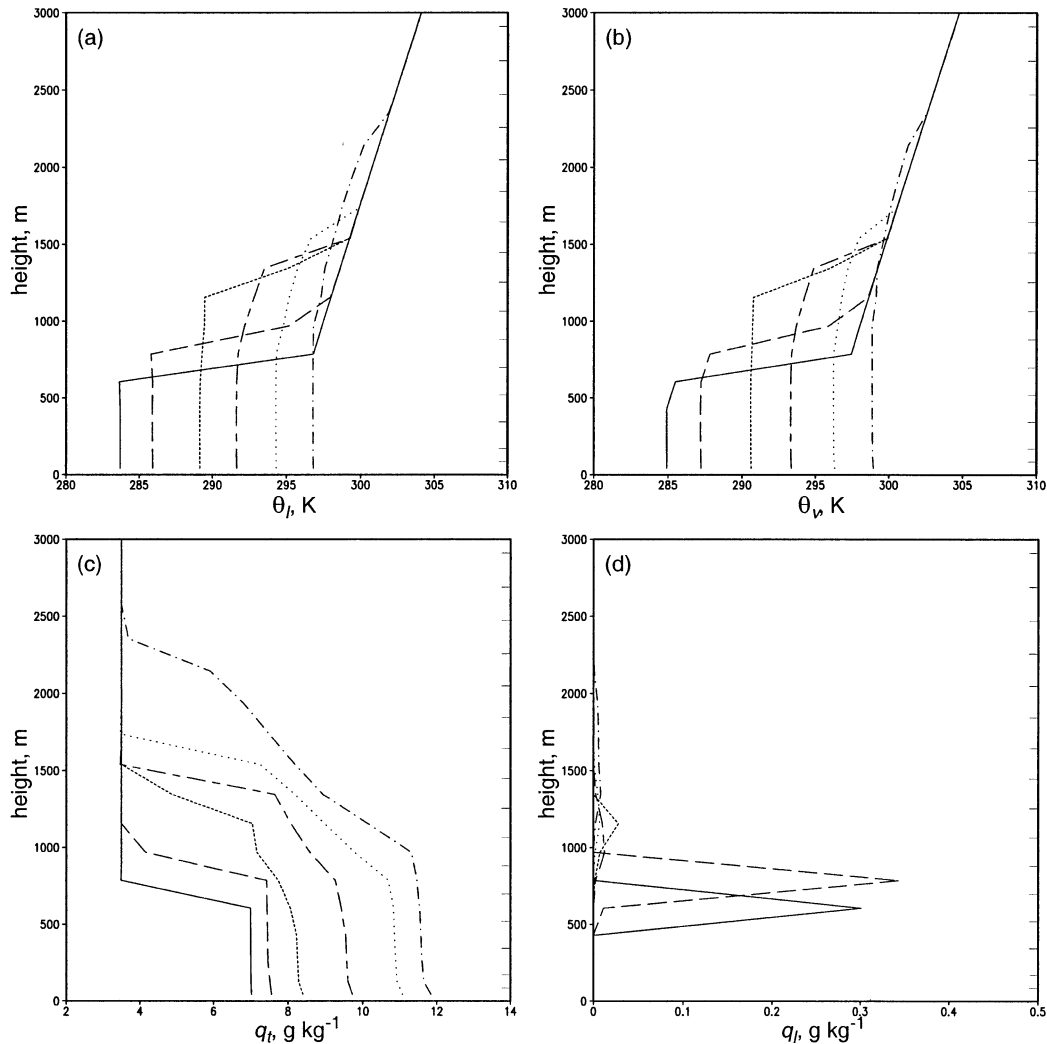

FIG. 9. Vertical profiles from the Lagrangian warming simulation at day 0 (solid), day 2 (dashed), day 4 (short dashed), day 6 (long–short dashed), day 8 (dotted), and day 10 (dashed–dotted): (a) θ_l, (b) θ_v, (c) q_t, and (d) q_l.
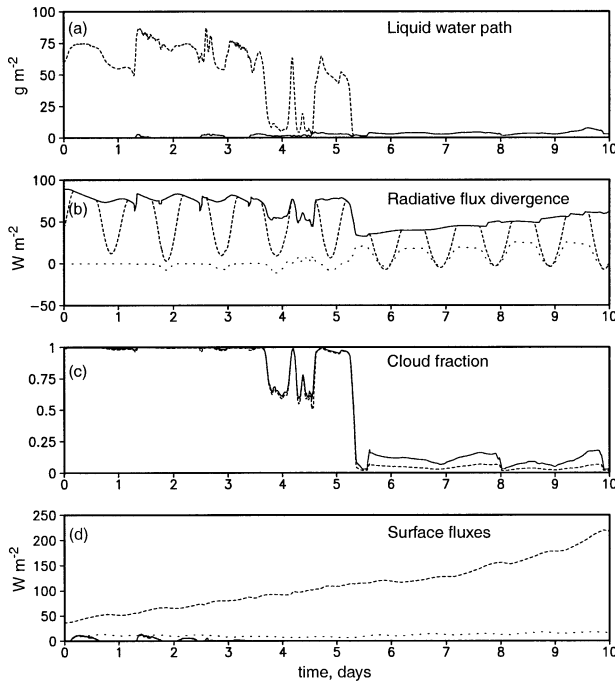
FIG. 10. Time series data from the Lagrangian warming simulation. From top to bottom are (a) explicitly resolved cloud water (dashed) and cumulus cloud water (solid); (b) longwave cooling of the boundary layer (solid), net radiative boundary layer cooling (dashed), and net radiative cooling of the surface mixed layer (dotted); (c) cloud fraction from the statistical scheme for random overlap assumption (solid) and maximum random overlap assumption (dashed); and (d) surface fluxes (W m^{-2}) of latent heat (dashed), sensible heat (dotted), and precipitation (solid).

start of the simulation to 2 K by the end. The θ_v soundings are moist adiabatic up to the trade inversion on days 0 to 4, then are weakly stable in the cumulus layer on days 6–10. The distribution of q_t more clearly shows a mixed layer with a strong gradient developing above after day 2. Considerable cloud water is present through day 2. This is predominantly cloud resolved by the model grid layers. Afterward, cumulus cloud water not exceeding 0.02 g kg^{-1} (grid cell mean) is present. This can also be seen clearly in Fig. 10a, which shows a time series of liquid water path for explicitly resolved and cumulus clouds. There is a slight diurnal variation in the liquid water path over the first day, with the expected midday minimum. After that, variations in the liquid water path correspond more closely to the trade-inversion jumping between model layers than to the time of day.

Radiative cooling near the marine-layer top is the principal process destabilizing the layer and driving the turbulent circulations. Longwave and net (longwave plus shortwave) radiative flux divergence within the diagnosed boundary layer (the surface to the lowest flux level within the trade inversion) are shown in Fig. 10b, along with net radiative flux divergence in the subcloud layer. Longwave cooling varies between 70 and 90 W

m^{-2} for the first 5 days and, during the breakup of the cloud, drops quickly to 30 W m^{-2}. The slow rise thereafter is due to the continued warming and deepening of the boundary layer. The initial smallness of the subcloud radiative cooling shows that cooling is concentrated at the stratocumulus cloud tops. There is a strong daytime reduction in the net boundary layer flux divergence due to shortwave absorption, but net radiative warming only occurs after the breakup of the cloud on day 5. During the cumulus phase of the simulation the solar absorption remains strong. This is in part due to clear-air absorption but may also be artificially enhanced by assuming pure random cloud overlap in the calculation of shortwave fluxes, as the radiatively active shallow cumulus occupy a small area fraction, but extend over several model levels. Figure 10c shows the diagnosed column cloud fraction from the statistical cloud scheme using a random overlap assumption (as in the shortwave radiative transfer parameterization) and a maximum random overlap assumption (as in the longwave parameterization). In the cumulus regime, the former gives cloud fractions of 10%–20%, more than twice as large as the latter.

Surface fluxes are shown in Fig. 10d. The sensible heat flux remains small throughout the simulation and does not exceed 20 W m^{-2}. The latent heat flux increases linearly from 40 W m^{-2} initially to 130 W m^{-2} on day 7, then ascends more steeply to 220 W m^{-2} by the end of day 10. Precipitation at the surface, shown as an equivalent heat flux, diminishes from 10 W m^{-2} initially to 0 on the third day. There is no precipitation from the shallow cumulus scheme.

3) SENSITIVITY STUDIES

(i) No shallow cumulus parameterization

To investigate the impact of the shallow cumulus scheme, the control case was run with the same forcings but with the shallow cumulus parameterization turned off. The time evolution of the resulting simulation is shown in Fig. 11. The first 2 days are nearly identical to the previous simulation. However, after the boundary layer begins to decouple, stratocumulus persists steadily through day 7. The TKE field shows periodic coupling and decoupling of the cloud and subcloud layers during this period. Over the last 3 days the resolved cloud is associated with discrete mixing events, as the model replaces the spatial variability of cumulus convection with temporal variability in the form of columnwide but intermittent diffusion. That this is not an efficient mechanism is shown by the depth of the surface mixed layer, which reaches 1300 m.

(ii) Decreased cloud droplet concentration

As was seen in Fig. 10, precipitation production is a substantial term in the heat budget of the boundary layer for the first several days. Since the associated latent heat release occurs within the cloud at the top of the bound-
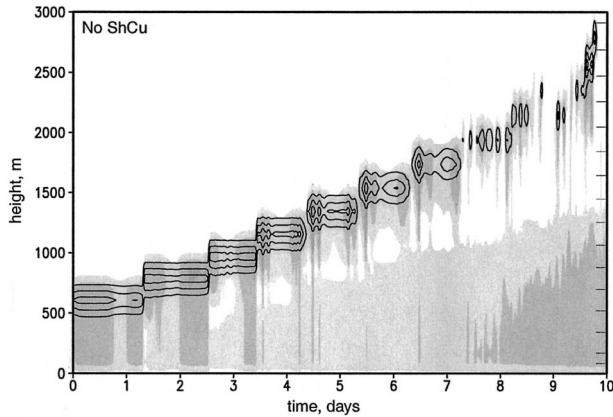
FIG. 11. Lagrangian warming case with no shallow cumulus: time evolution of TKE (shaded; contour interval 0.2 m^{-2} s^{-2}) and cloud water (black contours; interval 0.1 g kg^{-1}).

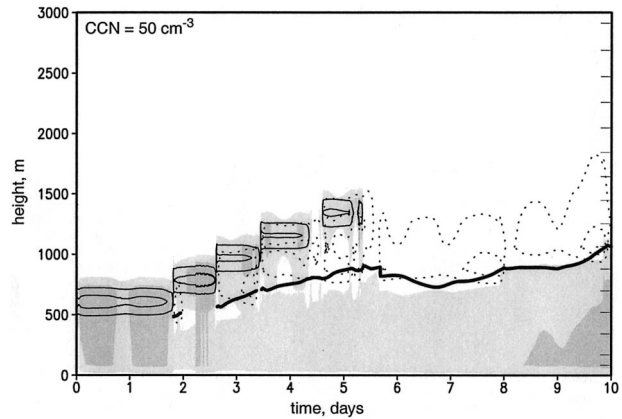FIG. 12. Lagrangian warming case with CCN of 50 cm^{-3}: time evolution of TKE (shaded; contour interval 0.2 m^{-2} s^{-2}), cloud water (thin black contours; interval 0.1 g kg^{-1}), cumulus mass flux (dotted contours; interval 0.02 kg m^{-2} s^{-1}), and cumulus cloud base (heavy solid line).

ary layer, it increases the boundary layer stratification, reducing turbulence and decreasing entrainment mixing. Figure 12 shows a time–height cross section of cloud water, cumulus mass flux, and TKE for a simulation with the cloud droplet concentration decreased from 100 to 50 cm^{-3}. This increases the autoconversion of cloud liquid water mixing ratio, whose rate is assumed to depend on the mean cloud droplet radius (Chen and Cotton 1987). The corresponding enhancement of precipitation decreases the liquid water path in the explicitly resolved stratocumulus layer by 40%; maximum liquid water contents in Fig. 12 are 0.25 g kg^{-1}, compared to 0.35 g kg^{-1} in the control run (Fig. 8).

Because of the increase in precipitation warming, and despite a decrease in shortwave absorption from the decreased liquid water path (not shown), the growth of the boundary layer is slower over the first 2 days of the simulation relative to the control case. The cloud height then increases rapidly, during the cumulus-under-stratocumulus phase. After the breakup of the stratiform cloud on day 6, the depth and structure of the boundary layer are quite similar to the original simulation.

(iii) Sensitivity to penetrative mixing coefficient

As discussed in section 2, the lateral mixing rate for cumulus updrafts is enhanced within the trade inversion by the penetrative mixing factor $r_p = 10.0$. To demonstrate the model sensitivity to r_p, the simulation was repeated with $r_p = 5.0$. The resulting time–height cross section is shown in Fig. 13. The beginning of the simulation is identical to the control case, but the duration of the transition from stratocumulus to cumulus is extended, and complete breakup does not occur until day 7. This is closer to the LES results of W97; however, the decreased penetrative mixing produces an excessively sharpened inversion in the BOMEX simulation.

4. Conclusions

We present a new mass flux parameterization of shallow cumulus convection and couple it to the GB01 PBL parameterization, which specifies vertical fluxes of conserved variables for turbulent layers through eddy diffusion. Our goal is to better represent cloud-topped boundary layers over the tropical and subtropical oceans and their radiative impacts on earth's climate. As the nature of the turbulence is very different in a dry convective subcloud layer and in a cumulus layer, the use of two different parameterizations to represent the turbulent transports in these two layers is a sensible choice, though a unified scheme (e.g., Lappen and Randall 2001) is also appealing.

The mass flux parameterization is based on the KF90 entraining–detraining plume model of a cumulus cloud ensemble and uses buoyancy sorting to specify detrain-
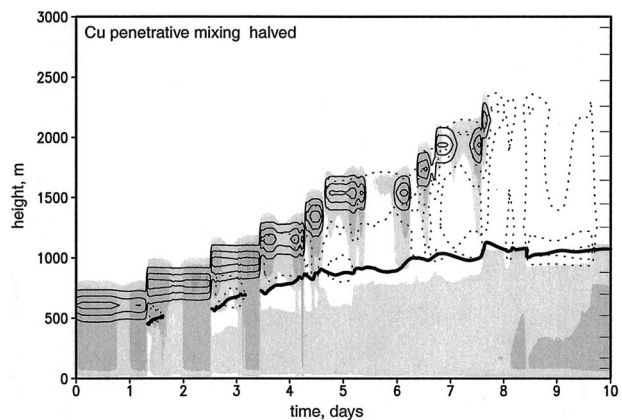

FIG. 13. Lagrangian warming case with $r_p = 5$: time evolution of TKE (shaded; contour interval 0.2 m^{-2} s^{-2}), cloud water (thin black contours; interval 0.1 g kg^{-1}), cumulus mass flux (dotted contours; interval 0.02 kg m^{-2} s^{-1}), and cumulus cloud base (heavy solid line).

ment. Novel features include a representation for penetrative mixing and a CIN-based closure for cloud-base mass flux. We have evaluated the model performance using single-column model simulations at relatively high vertical resolution. We focused on two cases, relevant to subtropical and tropical cloud-topped boundary layers, comprising 1) a pure trade-cumulus regime and 2) a cumulus to stratocumulus transition. The model maintains a cumulus field under the steady idealized conditions of the BOMEX simulation, while producing vertical fluxes and thermodynamic profiles in good agreement with the LES results. In the Lagrangian warming case, the model transitions from stratocumulus to cumulus in the expected manner, though slightly abruptly. The timing and duration of the transition are affected by several of the model parameters, including the TCM entrainment closure, the formulation of cumulus penetrative mixing, and drizzle microphysics.

The SCM has proven useful in exploring model sensitivities prior to the implementation of the parameterizations in a full three-dimensional model. While there are limitations in analyzing the parameterization in the SCM, it permits the evaluation of the model against LES results for the idealized cases, and the development of the parameterizations within the 1D MM5 permits the same source code to be used for 3D simulations. A companion paper (McCaa and Bretherton 2004) demonstrates the performance of the model in three-dimensional regional climate simulations over the northeast and southeast Pacific Ocean.

APPENDIX A

Mass Flux Equations

It is useful to rewrite the continuous set of equations for the updraft mass flux and thermodynamic state such that they can be accurately discretized in the vertical direction without constraints on the vertical grid spacing. Using the equality

$$\frac{\partial}{\partial z}(\psi_u e^{\varepsilon z}) = e^{\varepsilon z}\left(\varepsilon \psi_u + \frac{\partial \psi_u}{\partial z}\right), \qquad (A1)$$

the updraft dilution equation (14) can be rewritten

$$\frac{\partial}{\partial z}(\psi_u e^{\varepsilon z}) = (\varepsilon \overline{\psi} + S_u)e^{\varepsilon z}. \qquad (A2)$$

The vertical velocity equation can similarly be written as

$$\frac{\partial}{\partial z}(w_u^2 e^{2b\varepsilon z}) = 2aB_u e^{2b\varepsilon z}. \qquad (A3)$$

Discretized mass flux equations are derived by assuming entrainment and detrainment rates are constant within model layers. Integer subscripts are used to denote model thermodynamic levels, with flux levels indicated as half levels. The difference operator at level j is defined as $\Delta X_j = X_{j+1/2} - X_{j-1/2}$, and the thicknesses of the thermodynamic layers are $\Delta_j z$. During the ascent from $z_{j-1/2}$ to $z_{j+1/2}$ the plume is assumed to entrain air from the environment at a rate ε_j and detrain at a rate δ_j. Hence, one can integrate (13) from $z_{j-1/2}$ to $z_{j+1/2}$ to obtain the discretized mass flux equation

$$M_{u,j+1/2} = M_{u,j-1/2}e^{(\varepsilon_j - \delta_j)\Delta_j z}. \qquad (A4)$$

Similarly, since $\overline{\psi}$ represents the mean properties of environment air entrained into the updraft between $z_{j-1/2}$ and $z_{j+1/2}$, the updraft dilution equation becomes

$$\psi_{u,j+1/2} = \psi_{u,j-1/2}e^{-\varepsilon_j\Delta_j z}$$
$$+ (1 - e^{-\varepsilon_j\Delta_j z})(\overline{\psi} + S_\psi/\varepsilon_j). \qquad (A5)$$

The updraft and environmental θ_v at each flux level are computed from conserved variables by first-order Taylor expansion of the saturation mixing ratio at the liquid water temperature. Environmental values are computed using the finite-volume element interpretation of the profiles of conserved variables as suggested in GB01. Buoyancy of the updraft compared to the environment is assumed to vary linearly between $z_{j-1/2}$ and $z_{j+1/2}$ (note that, therefore, B_u is discontinuous on the flux levels). With these assumptions, integration of (A3) leads to

$$w_{u,j+1/2}^2 = w_{u,j-1/2}^2 e^{-2b\varepsilon_j\Delta_j z} + \frac{a\Delta_j B_u}{b\varepsilon_j}$$
$$+ \frac{a(1 - e^{-2b\varepsilon_j\Delta_j z})}{b\varepsilon_j}\left(B_{u,j-1/2} - \frac{a\Delta_j B_u}{2b\varepsilon_j\Delta_j z}\right). \quad (A6)$$

In the limit of no entrainment, (A3) can be integrated with $\varepsilon_j = 0$ to yield

$$w_{u,j+1/2}^2 = w_{u,j-1/2}^2 + a(B_{u,j-1/2} + B_{u,j+1/2})\Delta_j z. \quad (A7)$$

From boundary conditions at the base of the cumulus layer, these discrete equations provide values of the mass flux and updraft properties at the flux levels. If at the given level the updraft buoyancy is negative, then a closure for cumulus penetrative mixing (described in appendix D) is applied.

APPENDIX B

Computation of Critical Updraft Mixing Fraction

To determine the lateral entrainment and detrainment rates, a critical updraft mixing fraction χ_c is computed. This represents the mixture with the largest fraction of
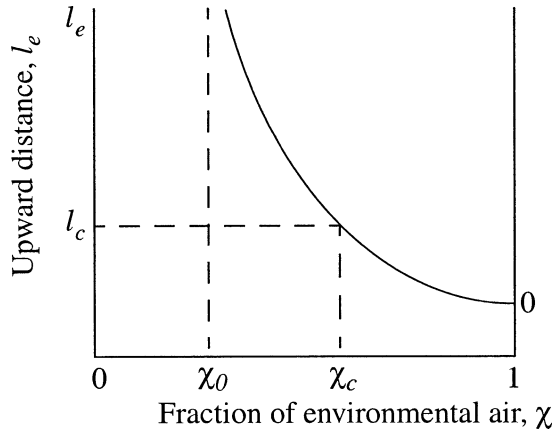
FIG. B1. Distance traveled upward by mixtures of updraft and environmental air, assuming a constant environment, where χ_0 indicates the fraction below which mixtures are positively buoyant with respect to the environment, and χ_c indicates the fraction below which mixtures are considered to be entrained into the updraft.

environmental air that will be entrained. To obtain χ_c, we first find the mixing fraction that yields parcels that are neutrally buoyant with respect to the environment. The virtual potential temperature for a saturated mixture containing the fraction χ of environmental air is computed following Randall (1980) using a linear combination of the differences of updraft and environmental θ_l and q_t,

$$\theta_v(\chi) = \theta_{vu} + \chi\left[\beta(\overline{\theta_l} - \theta_{l,u}) - \left(\frac{\beta L}{c_p \Pi} - \theta_u\right)(\overline{q_t} - q_{t,u})\right], \quad \text{(B1)}$$

where β is a thermodynamic coefficient dependent on temperature and pressure defined by Randall.

Given the buoyancy of a parcel, and assuming no additional entrainment, (A7) can be solved for the distance l_e the parcel will travel before stopping. Figure B1 shows l_e for typical mixtures of updraft and environmental air, where χ_c indicates the mixing fraction associated with a parcel that travels exactly the critical distance l_c described in (19). Only those parcels with environmental mixing fraction less than χ_c are included in the updraft.

APPENDIX C

Computation of the Convective Inhibition and Critical Velocity

To compute the CIN, it is necessary to specify the profiles of $\overline{\theta_v}$ and $\theta_{u,u}$ over the region where the updraft buoyancy is negative. Since the inversion is constrained to lie on a flux level, CIN is computed from this point to the level of free convection. For the environment, $\overline{\theta_v}$ is diagnosed just above and below each flux level,

and at the LCL, using the profiles of conserved variables. For the updraft, we assume ascent along the dry adiabat up to the LCL, and along the moist adiabat up to the LFC

$$\theta_{v,u}(p) = \overline{\theta_{vl,\text{inv}}} + \begin{cases} 0 & p \geq p_{\text{LCL}} \\ \gamma_m(p - p_{\text{LCL}}) & p < p_{\text{LCL}}, \end{cases} \quad \text{(C1)}$$

with γ_m the moist adiabatic lapse rate of θ_v. With these profiles, the parcel buoyancy is a linear function of p and the CIN can be obtained in a straightforward manner (see Fig. 2):

$$\text{CIN} = [B_u(p_{\text{inv}}) + B_u(p_{\text{LCL}})]\frac{p_{\text{LCL}} - p_{\text{inv}}}{g(\rho_{\text{LCL}} + \rho_{\text{inv}})}$$

$$+ B_u(p_{\text{LCL}})\frac{p_{\text{LFC}} - p_{\text{LCL}}}{g(\rho_{\text{LFC}} + \rho_{\text{LCL}})}, \quad \text{(C2)}$$

with the pressure of the LFC obtained as

$$p_{\text{LFC}} = p_{\text{inv}} - \frac{\Delta\overline{\theta_{vl}} + \gamma_e(p_{\text{inv}} - p_{\text{LCL}})}{\gamma_m - \gamma_e}, \quad \text{(C3)}$$

where γ_e is the lapse rate of θ_v in the environment. If the LFC lies above the next flux level (as shown in Fig. 2), the CIN is summed piecewise from the inversion to the LFC. The critical velocity can now be obtained by setting the left-hand side of (A7) to 0 and solving for w_c over a layer defined by the inversion at the bottom and the LFC at the top, yielding

$$w_c^2 = 2a(\text{CIN}). \quad \text{(C4)}$$

APPENDIX D

Implementation of Cumulus Penetrative Mixing Closure

As convective updrafts rise beyond their level of neutral buoyancy, they quickly decelerate and begin to descend. During this time they interact with inversion air through a combination of lateral and vertical mixing. To estimate the effective entrainment of inversion air through this process it is necessary to specify both the penetrative distance and the rate at which this mixing occurs.

Central to the computation of penetrative mixing is the estimation of the top (lowest) pressure p_t reached by the bulk updraft. Let the subscript d indicate the last layer in which the updraft is positively buoyant throughout, which is also the layer in which air from the overshooting, penetratively mixing updraft will be detrained. Then $p_{d+1/2} - p_t$ is the pressure distance within the inversion over which penetrative mixing will be considered. This represents the sum of the pressure thickness of each complete model layer that the updraft rises through above level d, plus some fractional distance that it penetrates the layer in which it stops. An expression for that fractional distance p_f is obtained by integrating

(A3) in the limit of no entrainment from the lower flux level of the layer to the point at which the updraft stops. This yields the quadratic equation

$$\left(\frac{B_{u,j+1/2} - B_{u,j-1/2}}{p_{j+1/2} - p_{j-1/2}}\right)p_f^2 + 2B_{u,j-1/2}p_f - g\overline{\rho_j}w_{u,j-1/2} = 0. \tag{D1}$$

Having found $p_t = p_{j-1/2} + p_f$, the penetrative mixing mass flux is specified at each flux level from d to the highest reached by the updraft as

$$M_e = -M_u(p_{k+1/2} - p_t)\varepsilon_i, \tag{D2}$$

with ε_i given in (29). The properties of the entraining air are computed at each flux level as a pressure-weighted average of the environmental air brought down from above.

REFERENCES

Arakawa, A., and W. H. Schubert, 1974: Interaction of a cumulus cloud ensemble with the large-scale environment, Part I. *J. Atmos. Sci.,* **31,** 674–701.

Bechtold, P., E. Bazile, F. Guichard, P. Mascart, and E. Richard, 2001: A mass-flux convection scheme for regional and global models. *Quart. J. Roy. Meteor. Soc.,* **127,** 869–886.

Betts, A. K., 1973: Non-precipitating cumulus convection and its parameterization. *Quart. J. Roy. Meteor. Soc.,* **99,** 178–196.

——, 1986: New convective adjustment scheme, Pt. 1, Observational and theoretical basis. *Quart. J. Roy. Meteor. Soc.,* **112,** 677–691.

Carpenter, R. L., Jr., K. K. Droegemeier, and A. A. Blyth, 1998: Entrainment and detrainment in numerically simulated cumulus congestus clouds. Part III: Parcel analysis. *J. Atmos. Sci.,* **55,** 3434–3455.

Chen, C., and W. R. Cotton, 1987: The physics of the marine stratocumulus-capped mixed layer. *J. Atmos. Sci.,* **44,** 2951–2977.

de Roode, S. R., and C. S. Bretherton, 2003: Mass-flux budgets of shallow cumulus clouds. *J. Atmos. Sci.,* **60,** 137–151.

Emanuel, K. A., 1991: A scheme for representing cumulus convection in large-scale models. *J. Atmos. Sci.,* **48,** 2313–2335.

——, and D. J. Raymond, 1992: Report from a workshop on cumulus parameterization. *Bull. Amer. Meteor. Soc.,* **73,** 318–325.

Esbensen, S., 1978: Bulk thermodynamic effects and properties of small tropical cumuli. *J. Atmos. Sci.,* **35,** 826–837.

Fairall, C. W., E. F. Bradley, D. P. Rogers, J. B. Edson, and G. S. Young, 1996: Bulk parameterization of air–sea fluxes for Tropical Ocean–Global Atmosphere Coupled-Ocean Atmosphere Response Experiment. *J. Geophys. Res.,* **101,** 3747–3764.

Galperin, B., L. H. Kantha, S. Hassid, and A. Rosati, 1988: A quasi-equilibrium turbulent energy model for geophysical flows. *J. Atmos. Sci.,* **45,** 55–62.

Grant, A. L. M., and A. R. Brown, 1999: A similarity hypothesis for shallow-cumulus transports. *Quart. J. Roy. Meteor. Soc.,* **125,** 1913–1936.

Gregory, D., 2001: Estimation of entrainment rate in simple models of convective clouds. *Quart. J. Roy. Meteor. Soc.,* **127,** 53–72.

——, and P. R. Rowntree, 1990: A mass flux convection scheme with representation of cloud ensemble characteristics and stability-dependent closure. *Mon. Wea. Rev.,* **118,** 1483–1506.

——, R. Kershaw, and P. M. Iness, 1997: Parameterization of momentum transport by convection. Part II: Tests in single-column and general circulation models. *Quart. J. Roy. Meteor. Soc.,* **123,** 1153–1183.

Grell, G. A., J. Dudhia, and D. R. Stauffer, 1994: A description of the fifth generation Penn State/NCAR Mesoscale Model (MM5).

National Center for Atmospheric Research Tech. Note NCAR/TN-398, 80 pp.

Grenier, H., and C. S. Bretherton, 2001: A moist PBL parameterization for large-scale models and its application to subtropical cloud-topped marine boundary layers. *Mon. Wea. Rev.,* **129,** 357–377.

Holland, J. Z., and E. M. Rasmusson, 1973: Measurements of the atmospheric mass, energy, and momentum budgets over a 500-kilometer square of tropical ocean. *Mon. Wea. Rev.,* **101,** 44–55.

Johnson, R. H., 1976: Role of convective-scale precipitation downdrafts in cumulus and synoptic-scale interactions. *J. Atmos. Sci.,* **33,** 1890–1910.

——, T. M. Rickenbach, S. A. Rutledge, P. E. Ciesielski, and W. H. Schubert, 1999: Trimodal characteristics of tropical convection. *J. Climate,* **12,** 2397–2418.

Kain, J. S., and J. M. Fritsch, 1990: A one-dimensional entraining/detraining plume model and its application in convective parameterization. *J. Atmos. Sci.,* **47,** 2784–2802.

Krueger, S. K., G. T. McLean, and Q. Fu, 1995: Numerical simulation of the stratus-to-cumulus transition in the subtropical marine boundary layer. Part I: Boundary-layer structure. *J. Atmos. Sci.,* **52,** 2839–2850.

——, C.-W. Su, and P. A. McMurtry, 1997: Modeling entrainment and finescale mixing in cumulus clouds. *J. Atmos. Sci.,* **54,** 2697–2712.

Lappen, C. L., and D. A. Randall, 2001: Toward a unified parameterization of the boundary layer and moist convection. Part I: A new type of mass-flux model. *J. Atmos. Sci.,* **58,** 2021–2036.

Lin, C., 1999: Some bulk properties of cumulus ensembles simulated by a cloud-resolving model. Part I: Cloud root properties. *J. Atmos. Sci.,* **56,** 3724–3735.

——, and A. Arakawa, 1997a: The macroscopic entrainment processes of simulated cumulus ensemble. Part I: Entrainment sources. *J. Atmos. Sci.,* **54,** 1027–1043.

——, and ——, 1997b: The macroscopic entrainment processes of simulated cumulus ensemble. Part II: Testing the entraining-plume model. *J. Atmos. Sci.,* **54,** 1044–1053.

Mapes, B. E., 2000: Convective inhibition, subgrid-scale triggering energy, and stratiform instability in a toy tropical wave model. *J. Atmos. Sci.,* **57,** 1515–1535.

McCaa, J. R., 2001: A new parameterization of marine stratocumulus and shallow cumulus clouds for climate models. Ph.D. dissertation, University of Washington, 161 pp.

——, and C. S. Bretherton, 2004: A new parameterization for shallow cumulus convection and its application to marine subtropical cloud-topped boundary layers. Part II: Regional simulations of marine boundary layer clouds. *Mon. Wea. Rev.,* **132,** 883–896.

Mellor, G. L., and T. Yamada, 1982: Development of a turbulence closure model for geophysical fluid problems. *Rev. Geophys. Space Phys.,* **20,** 851–875.

Nicholls, S., M. A. LeMone, and G. Sommeria, 1982: Simulation of a fair weather marine boundary layer in GATE using a three-dimensional model. *Quart. J. Roy. Meteor. Soc.,* **108,** 167–190.

Nitta, T., and S. Esbensen, 1974: Heat and moisture budget analyses using BOMEX data. *Mon. Wea. Rev.,* **102,** 17–28.

Norris, J. R., 1999: On trends and possible artifacts in global ocean cloud cover between 1952 and 1995. *J. Climate,* **12,** 1864–1870.

Paluch, I. R., 1979: Entrainment mechanism in Colorado cumuli. *J. Atmos. Sci.,* **36,** 2467–2478.

Pennell, W. T., and M. A. LeMone, 1974: An experimental study of turbulence structure in the fair-weather trade wind boundary layer. *J. Atmos. Sci.,* **31,** 1308–1323.

Pielke and Coauthors, 1992: A comprehensive meteorological modeling system—RAMS. *Meteor. Atmos. Phys.,* **49,** 69–91.

Raga, G. G., J. B. Jensen, and M. B. Baker, 1990: Characteristics of cumulus band clouds off the coast of Hawaii. *J. Atmos. Sci.,* **47,** 338–355.

Randall, D. A., 1980: Conditional instability of the first kind upside-down. *J. Atmos. Sci.,* **37,** 125–130.

Raymond, D. J., and A. M. Blyth, 1986: A stochastic mixing model for nonprecipitating cumulus clouds. *J. Atmos. Sci.,* **43,** 2708–2718.

Reuter, G. W., and M. K. Yau, 1987: Mixing mechanisms in cumulus congestus clouds. Part II: Numerical simulations. *J. Atmos. Sci.,* **44,** 798–827.

Siebesma, A. P., 1998: Shallow cumulus convection. *Buoyant Convection in Geophysical Flows,* E. J. Plate et al., Eds., Kluwer, 441–486.

——, and J. W. M. Cuijpers, 1995: Evaluation of parametric assumptions for shallow cumulus convection. *J. Atmos. Sci.,* **52,** 650–666.

——, and A. A. M. Holtslag, 1996: Model impacts of entrainment and detrainment rates in shallow cumulus convection. *J. Atmos. Sci.,* **53,** 2354–2364.

——, and Coauthors, 2003: A large eddy simulation intercomparison study of shallow cumulus convection. *J. Atmos. Sci.,* **60,** 1201–1219.

Simpson, J., and V. Wiggert, 1969: Models of precipitating cumulus towers. *Mon. Wea. Rev.,* **97,** 471–489.

Stevens, B., 2000: Cloud-transitions and decoupling in shear-free stratocumulus topped boundary layers. *Geophys. Res. Lett.,* **27,** 2557–2560.

Taylor, G. R., and M. B. Baker, 1991: Entrainment and detrainment in cumulus clouds. *J. Atmos. Sci.,* **48,** 112–120.

Tiedtke, M., 1989: A comprehensive mass flux scheme for cumulus parameterization in large-scale models. *Mon. Wea. Rev.,* **117,** 1779–1800.

——, W. A. Heckley, and J. Slingo, 1988: Tropical forecasting at ECMWF: The influence of physical parameterization on the mean structure of forecasts and analyses. *Quart. J. Roy. Meteor. Soc.,* **114,** 639–644.

Telford, J. W., 1975: Turbulence, entrainment, and mixing in cloud dynamics. *Pure Appl. Geophys.,* **113,** 1067–1084.

von Salzen, K., and N. A. McFarlane, 2002: Parameterization of the bulk effects of lateral and cloud-top entrainment in transient shallow cumulus clouds. *J. Atmos. Sci.,* **59,** 1405–1430.

Wyant, M. C., C. S. Bretherton, H. A. Rand, and D. E. Stevens, 1997: Numerical simulations and a conceptual model of the stratocumulus to trade cumulus transition. *J. Atmos. Sci.,* **54,** 168–192.

Yanai, M., S. Esbensen, and J. Chu, 1973: Determination of bulk properties of tropical cloud clusters from large-scale heat and moisture budget. *J. Atmos. Sci.,* **30,** 611–627.